

# Journal of Biomedical Optics

BiomedicalOptics.SPIEDigitalLibrary.org

## Characterization of laser ultrasound source signals in biological tissues for imaging applications

Jonathan R. Fincke  
Charles M. Wynn  
Rob Haupt  
Xiang Zhang  
Diego Rivera  
Brian Anthony

**SPIE.**

Jonathan R. Fincke, Charles M. Wynn, Rob Haupt, Xiang Zhang, Diego Rivera, Brian Anthony,  
“Characterization of laser ultrasound source signals in biological tissues for imaging applications,”  
*J. Biomed. Opt.* **24**(2), 021206 (2018), doi: 10.1117/1.JBO.24.2.021206.

# Characterization of laser ultrasound source signals in biological tissues for imaging applications

Jonathan R. Fincke,<sup>a,b,\*</sup> Charles M. Wynn,<sup>c</sup> Rob Haupt,<sup>c</sup> Xiang Zhang,<sup>a,b</sup> Diego Rivera,<sup>c</sup> and Brian Anthony<sup>a,b</sup>

<sup>a</sup>Massachusetts Institute of Technology, Department of Mechanical Engineering, Cambridge, Massachusetts, United States

<sup>b</sup>Institute for Medical Engineering and Science (IMES), Massachusetts Institute of Technology, Cambridge, Massachusetts, United States

<sup>c</sup>Massachusetts Institute of Technology, Lincoln Laboratory, Lexington, Massachusetts, United States

**Abstract.** Short optical pulses emitted from a tunable Q-switched laser (800 to 2000 nm) generate laser ultrasound (LUS) signals at the surface of biological tissue. The LUS signal's acoustic frequency content, dependence on sample type, and optical wavelength are observed in the far field. The experiments yield a reference dataset for the design of noncontact LUS imaging systems. Measurements show that the majority of LUS signal energy in biological tissues is within the 0.5 and 3 MHz frequency bands and the total acoustic energy generated increases with the optical absorption coefficient of water, which governs tissue optical absorption in the infrared range. The experimental results also link tissue surface roughness and acoustic attenuation with limited LUS signal bandwidth in biological tissue. Images constructed using 810-, 1064-, 1550-, and 2000-nm generation laser wavelengths and a contact piezoelectric receiver demonstrates the impact of the generation laser wavelength on image quality. A noncontact LUS-based medical imaging system has the potential to be an effective medical imaging device. Such a system may mitigate interoperator variability associated with current medical ultrasound imaging techniques and expand the scope of imaging applications for ultrasound. © The Authors. Published by SPIE under a Creative Commons Attribution 4.0 Unported License. Distribution or reproduction of this work in whole or in part requires full attribution of the original publication, including its DOI. [DOI: [10.1117/1.JBO.24.2.021206](https://doi.org/10.1117/1.JBO.24.2.021206)]

Keywords: laser ultrasound; ultrasound; tunable laser; optoacoustic; medical imaging; acoustic source.

Paper 180242SSR received Apr. 25, 2018; accepted for publication Nov. 7, 2018; published online Dec. 8, 2018.

## 1 Introduction

A noncontact medical laser ultrasound (LUS) imaging system could deliver repeatable, quantitative (sound, speed, and density), and volumetric images without contacting or applying coupling material to the patient. An ultrasound system possessing any one of these attributes would be highly valuable to today's clinicians.<sup>1-7</sup> Potential applications for noncontact LUS in the medical setting include general clinical imaging, monitoring bone, muscle health, organ health, needle guidance, interoperative imaging, and aiding cancer detection and screening.

Noncontact LUS systems, like those employed in nondestructive testing<sup>8-10</sup> (NDT), consist of a generation laser and detection laser. Conceptually, noncontact LUS is identical to conventional ultrasound except there is no coupling agent and the piezoelectric source/receiver is replaced with a generation laser (for ultrasound wave generation) and a detection laser (for ultrasound wave detection). The use of optical (laser) systems in LUS enables ultrasonic imaging of objects without contact. The generation laser is a pulsed laser that generates a propagating thermoelastic acoustic (compressional) and/or shear wave at the surface of a sample via the optoacoustic effect,<sup>11,12</sup> referred to here as the LUS source. The detection laser is a Doppler vibrometer (interferometer), which records direct or reflected LUS source waves (sensitive to sound speed and density distribution within the sample) at the surface of the sample.<sup>13-16</sup> All detection and generation of the acoustic waves occurs optically, without contact, at a distance, and without coupling agent or immersion of the sample. Images

from these systems display quantities related to the gradient of the sound speed and density distribution (pulse-echo reconstruction) or the sound speed and density distribution itself (tomographic reconstruction) within the sample to centimeter depths. LUS is similar to noncontact photoacoustic (PA) techniques in that both can employ pulsed lasers and laser Doppler interferometers; however, the two techniques image different physical properties within the medium. PA methods principally image optically absorptive structures within the sample volume,<sup>17</sup> whereas LUS images sound speed and density inhomogeneity in the sample volume.

A number of industries successfully utilize noncontact LUS techniques for NDT applications such as aerospace composite inspection, steel pipe thickness measurement, and assessment of microelectronic thin-film thickness among others.<sup>9</sup> Recent research in noncontact LUS for medical imaging applications demonstrates promising proof of concept images obtained on phantoms and dead animal tissue.<sup>18-24</sup> Other researchers are developing contact or immersion medical imaging systems based on optoacoustic or LUS transducers comprised of materials, which enhance the optoacoustic effect.<sup>25-29</sup> While much of the LUS research for medical applications focuses on imaging, others investigated the near-field characteristics of LUS source signals in biological tissue over a range of optical wavelengths.<sup>30-35</sup> More recently, studies of the LUS source characteristics in the far field have been studied in tissue-mimicking phantoms, but these experiments have not evaluated effects due to the surface roughness of skin.<sup>24</sup>

This study also addresses LUS source characteristics in biological tissue by expanding the range of optical wavelengths and tissue types under test. Despite recent interest in noncontact LUS for medical imaging, there are few publications addressing

\*Address all correspondence to: Jonathan R. Fincke, E-mail: [jfincke@mit.edu](mailto:jfincke@mit.edu)

the characteristics of LUS source signals generated in biological tissues in the far field.<sup>24</sup> The LUS source characteristics are critical to designing noncontact LUS imaging systems as the source amplitude and bandwidth set bounds the resolution and penetration depth of the imaging system. The data from the study serve two purposes. (1) A reference dataset for the design of noncontact LUS imaging systems for biological tissue. (2) Further experimental evidence for using existing analytical LUS source theory<sup>11,12,36–42</sup> over a broad range of optical wavelengths and tissue types to predict LUS source characteristics in the far field.

The experiments employ an LUS generation laser to excite an LUS source at the surface of bovine shoulder muscle, pork hock, and skin-on chicken breast tissue samples. At the opposite surface of the tissue, a contact piezoelectric acoustic transducer records the LUS source waveform. The observational dataset consists of time-domain trace signals. Spectra and acoustic signal energy are calculated for all tissues, over optical wavelengths from 800 to 2000 nm at 50-nm increments. Comparison of measured time-domain signals, spectra, and signal energy to theoretical pure water models shows congruence between biological tissue experimental data and pure water models. The similarity between the observation and models indicates acoustic attenuation and surface roughness limit the bandwidth of the LUS source signal. Lastly, images constructed using 810-, 1064-, 1550-, and 2000-nm generation laser wavelengths demonstrate the impact of the generation laser wavelength on pulse-echo ultrasound image quality. The data acquisition to generate the images utilizes the conversion of the generation laser optical pulses into ultrasound waves via the optoacoustic effect at the tissue surface and a contact piezoelectric transducer to receive scattered and reflected ultrasound waves. The images are formed using synthetic aperture focusing techniques (SAFT) that focus the received time-domain acoustic backscatter and reflection signals back to their origin in space.<sup>10</sup> In contrast, conventional ultrasound imaging uses full piezoelectric arrays (not generation and/or detection lasers) that are mechanically coupled to the target with ultrasound gel to focus on the transmit and receive the resulting scattered and reflected ultrasound waves (no synthetic aperture).<sup>43</sup>

## 2 Methods

### 2.1 Theoretical Background

The relevant theory governing LUS signal generation in fluids is reviewed in the literature.<sup>11,12,36–40,42</sup> For a thorough theoretical explanation of LUS see Refs. 11 and 12. The physical mechanism for generating an LUS signal is summarized as follows: (1) a short duration laser pulse impinges on an optically absorptive surface of a material, such as water or biological tissue, (2) the optical energy rapidly and locally converts into localized heat at the laser spot location,<sup>44</sup> (3) nearly instantaneous expansion of the material due to the localized heating creates a concentration of mechanical stress within the irradiated material, and (4) this stress imbalance dissipates via the propagation of an acoustic pulse from the irradiated region into the material volume. The propagating acoustic pulse is the laser-induced ultrasound wave, the LUS source, which can be utilized for imaging. For this process to occur as described, optical, thermal, and acoustic conditions need to be met by the material and laser pulse. The most critical condition is being the significant absorption of optical energy at the sample surface, relative to optical transmission into the tissue.

This optical condition is described by the characteristic optical penetration depth of light into the material, defined by  $l$ , with units of (m), as shown in Fig. 1(a). The optical intensity, with units of (W/m<sup>2</sup>), of incident light as a function of depth into an absorptive and scattering medium is described as

$$U = U_o e^{-z(\mu_s + \mu_a)}, \quad (1)$$

where  $U_o$  is the incident intensity at the surface,  $z$  is the penetration depth into the tissue, and  $\mu_a$  and  $\mu_s$  are the optical absorption and scattering coefficients in the medium, respectively, with units of (m<sup>-1</sup>). The characteristic depth an optical beam will penetrate a medium is  $l = (\mu_s + \mu_a)^{-1}$  and for biological tissue at wavelengths >1400 nm, this depth is <1 mm, which is on the order of an acoustic wavelength used for medical ultrasound imaging.<sup>45,46</sup> The small optical penetration depth compared with typical imaging depths of 5 to 10 cm allows the assumption that the acoustic source is located at the surface of the material.

The thermal condition is the rate of thermal conduction within the material compared with heating time. By analyzing the diffusive terms in the heat equation,<sup>12</sup> one arrives at the equation

$$\tau \ll l_{\min}^2 \rho C_p / \kappa, \quad (2)$$

where  $\rho$  is the material density with units (kg/m<sup>3</sup>),  $C_p$  is the medium specific heat with units (J/kg K),  $\kappa$  is the thermal conductivity with units (W/m K),  $\tau$  is the laser pulse length in units of (s), and  $l_{\min}$  is the smaller of  $l$  or  $a$ , where  $a$  is the laser beam diameter with units of (m) [Fig. 1(a)]. This condition requires the heating time to be much shorter than the time for heat to conduct away from the heating zone in the material and allows for the assumption of instantaneous heating. The instantaneous heating gives rise to the local expansion of the material and the need for the localized stress or acoustic (source) condition.

The acoustic source condition requires what is often called “stress confinement” in the literature. Physically, this condition means that the mechanical energy generated by the thermal expansion of the material cannot propagate away quicker than the rate of energy delivery.

This condition requires

$$\tau \ll \frac{l}{c}, \quad (3)$$

$$\tau \ll \frac{a}{c}, \quad (4)$$

where  $c$  is the speed of sound in that material in (m/s). In the context of LUS, Eq. (4) requires the spot diameter and optical penetration depth to be sufficiently large to achieve these conditions.

When the conditions are met, an LUS acoustic source can be efficiently generated in biological tissue.<sup>21,30,31</sup> For biological tissues, with a sufficiently large laser spot diameter, all three conditions are met for optical wavelengths from 800 to 2000 nm.

Theoretical models for an LUS wave in pure water with a smooth surface show that the frequency-domain expression for the waveform is given by Eq. (5) in Ref. 12 and is presented again here with slightly different nomenclature as:

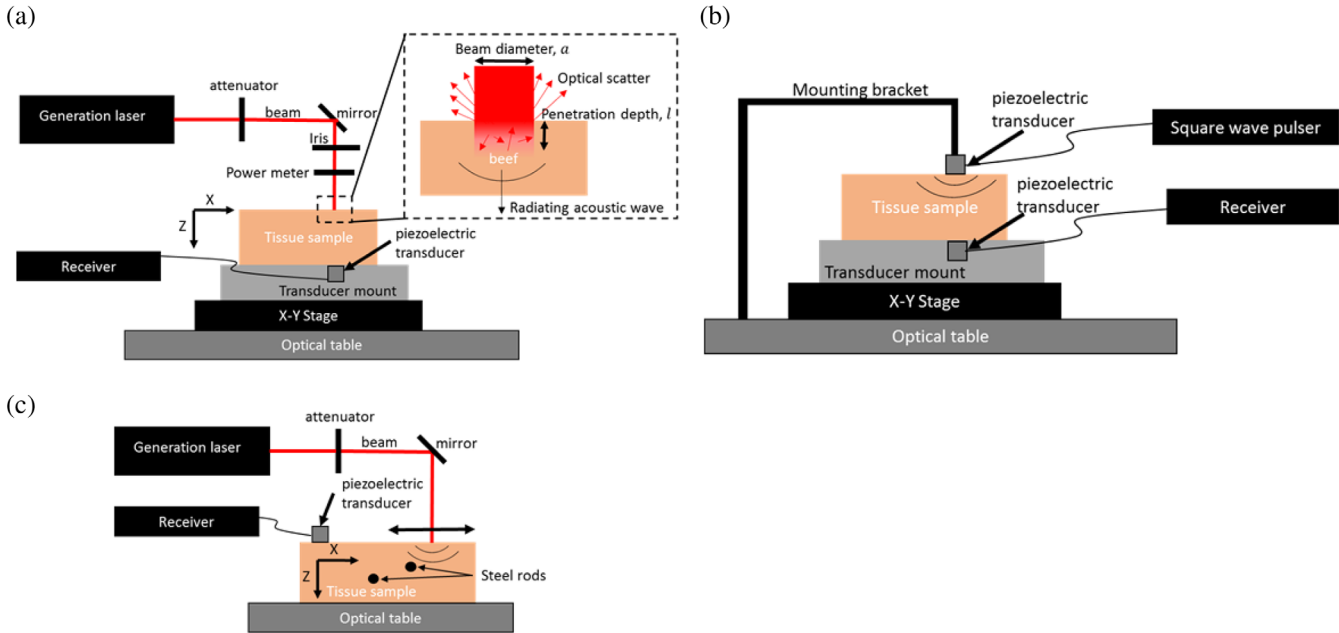


**Fig. 1** Schematic of the three experimental setups employed. (a) Experimental setup one: the generation laser is used to excite an acoustic wave at the surface of the tissue sample, which is detected by the piezoelectric transducer at the bottom of the sample. (b) Experimental setup two: a piezoelectric transducer is lightly contacted with the top of the tissue sample and emits an acoustic wave, which is detected by the piezoelectric transducer at the bottom of the sample. (c) Experimental setup three (imaging setup): the generation laser excites an acoustic wave at the surface of the tissue sample, which is detected by the piezoelectric transducer at the surface of the sample. The mirror scans the generation laser spot along the surface of the sample and the two steel rods serve as test targets.

$$P_s(\omega) = \frac{iU_o\beta\mu_a}{2C_p} \frac{e^{ikR}}{R} \frac{a^2k \cos(\theta)}{\mu_a^2 + k^2 \cos^2(\theta)} \exp\left(-\frac{a^2k^2 \sin^2(\theta)}{4}\right), \quad (5)$$

where  $\omega$  is the radian frequency,  $i$  is the imaginary unit,  $R$  is the range from the source to the target,  $\beta$  is the coefficient of thermal expansion in  $(\text{K}^{-1})$ ,  $\theta$  is the angle from the source to the target, and  $k$  is the acoustic wave number defined as  $k = 2\pi/\lambda$ , where  $\lambda$  is the acoustic wavelength (note:  $k = \omega/c$ ). The inverse Fourier transform of Eq. (5) yields the time-domain signal. The expression  $\frac{\mu_a k \cos(\theta)}{\mu_a^2 + k^2 \cos^2(\theta)}$  in Eq. (5) is an optical to acoustic conversion efficiency factor scaling the amplitude of the source signal as a function of acoustic frequency and  $\mu_a$ . Thus, the optical absorption can significantly impact the resultant acoustic frequency response. The average frequency-domain expression for the LUS waveform generated on a rough surface with a Gaussian distribution of roughness heights is given by Eq. (5) in Ref. 12 and is presented here with slightly different nomenclature as

$$\langle P_r(\omega) \rangle = P_s(\omega) \exp\left(-\frac{\sigma^2 k^2 \cos^2(\theta)}{2}\right), \quad (6)$$

where  $\sigma$  is the mean square height of the roughness with units of (m). The signal decays with increasing frequency scaled by  $\sigma$ . The impact of roughness can be significant. For example, for optical and acoustic parameters typical of biological tissue, a surface roughness with  $\sigma = 0.001$  m results in a 5-dB reduction in the source amplitude at 2.5 MHz compared with a smooth surface.

Acoustic attenuation,  $\alpha$ , is also important when using LUS to image biological tissue. Acoustic attenuation is due to heating and scattering within the tissue. In human tissue,  $\alpha = 0.5$  to 2 (dB/cm MHz) and in bovine muscle values of 2 to 3 (dB/cm MHz) have been reported.<sup>47,48</sup> Acoustic absorption impacts the depth- and frequency-dependent amplitude,  $A$ , of an acoustic wave exponentially, as given as

$$A(z, \omega) = A_o 10^{-\frac{\alpha z \omega}{40}}, \quad (7)$$

where  $A_o$  is the initial pressure amplitude, with units of (Pa). Acoustic attenuation, with respect to imaging, severely decreases the amplitude of high-frequency signals and limits spatial resolution. As image resolution is dependent on the inverse bandwidth of the transmit signal, attenuation can set an upper limit of image resolution and maximum imaging depth due to finite signal-to-noise ratio (SNR) of imaging systems.

## 2.2 Experimental Setup

Three hardware configurations [Figs. 1(a)–1(c)] are utilized for the experiments. The first configuration [Fig. 1(a)] uses the LUS generation laser for exciting an acoustic wave at the surface of the sample and the second configuration [Fig. 1(b)] uses a piezoelectric transducer to generate an acoustic wave at the surface of the sample. The second configuration is employed to isolate the impact of tissue surface roughness for comparison with data from configuration one. The third setup is a pulse echo imaging setup [Fig. 1(c)] that consists of an LUS generation laser to excite an LUS source at the surface and a contact piezoelectric transducer to receive the reflected and direct arrivals from the LUS source.

The generation laser is a Continuum 9030 Panther (30 pulses/s, 9 ns pulses) tunable optical parametric oscillator laser, operating at discrete optical wavelengths from 800 to 2000 nm stepped in 50-nm increments. About 2000 nm is the maximum wavelength used due to generation of laser hardware constraints and significant reductions in the acoustic source amplitude beyond 2000 nm. More specifically, the optical penetration depth becomes much smaller than the acoustic wavelengths of interest causing significant reductions in LUS source efficiency [see Eq. (5)] at the acoustic frequencies of interest (0.5 to 5.0 MHz). Further, theoretical exposure thresholds for skin are 10 times lower beyond 2600 nm. The beam from the laser passes through an adjustable attenuator to a mirror, which directs the beam through a 3-mm iris and then onto the sample. Beneath the iris is a removable power meter to measure the optical power reaching the sample [Fig. 1(a)]. The tissue sample lays underneath the iris on the transducer mounting-bracket, which is mounted on an  $x - y$  stage rigidly secured to the optical table [Fig. 1(a)]. The  $x - y$  stage enables centering of the laser spot above the piezoelectric acoustic receiving transducer (Olympus V1091). The transducer mount serves as a rigid mount for the transducer and Aquasonic<sup>R</sup> 100 ultrasound transmission gel couples the transducer to the tissue sample. The transducer has a 5-MHz center frequency and a usable bandwidth between 0.5 and 8.0 MHz. The piezoelectric, disk-shaped element in the transducer is 3.0 mm in diameter yielding a far-field distance of  $\sim 3$  cm at 5 MHz. A piezoelectric transducer is selected to measure the waveforms to avoid variability in vibrometer sensitivity and SNR due to variation in tissue optical properties between samples. A piezoelectric transducer guarantees consistent detection behavior across different tissue types and samples. After the waveform passes through an Olympus 5077 PR pulser-receiver with a 50-dB gain and a 10-MHz lowpass filter, a Tektronix TDS 2024B 200 MHz oscilloscope digitizes the waveform for collection.

The second setup uses two of the same piezoelectric transducers previously mentioned. The source-transducer connected to an Olympus 5077 PR pulser-receiver is mounted to an adjustable bracket fixed to the optical table. The pulser-receiver generates a one-and-a-half cycle square wave with 0.7- $\mu$ s duration peaks. The source transducer is centered above the receiving transducer and lightly contacted with the tissue sample using the adjustable mounting bracket. Ultrasound gel couples the source and receives transducers to the sample. The waveform acquisition setup and receiving transducer configuration are identical to the first setup.

Three sample types are tested, bovine muscle, chicken breast with skin, and a pork hock bought from the butcher and approved for use under Massachusetts Institute of Technology Committee on Animal Care protocol number E17-09-0320 for use of animal tissue. All tissue samples are at least 3.5 cm in height such that all data with frequency content  $< 5$  MHz are in the far field of both the transducer and LUS source. The bovine sample contains only muscle and fat, while the chicken and pork samples both have skin at the surface with muscle and fat tissue underneath.

The data collection process using the first setup starts by centering the laser spot above the transducer. Next, the generation laser wavelength is manually swept from 800 to 2000 nm at 50-nm increments. Across the spectrum of wavelengths, the laser power is kept at 7.5 mW with a spot area of 0.071 cm<sup>2</sup> (3-mm diameter) yielding a fluence of 3.54 mJ/cm<sup>2</sup> per

pulse, which is skin safe across the entire evaluated optical spectrum to avoid tissue damage. Consequently, this fluence level is also eye safe for wavelengths between 1500 and 1800 nm<sup>49</sup> with a safety factor just under 10 (30-Hz pulse frequency). The laser power at the samples remains constant by checking the power meter after changing the laser wavelength and correcting the attenuator as needed to maintain constant power.

At each optical wavelength, the LUS source generated by the laser pulse is saved on the oscilloscope for postprocessing, resulting in 25 waveforms for each tissue sample tested. Signals with insufficient SNR are omitted from the dataset.

The data collection process using the second setup starts by centering the source transducer above the receiving transducer. Next, an acoustic pulse propagates from the source transducer through the tissue to the receiving transducer. An oscilloscope attached to the receiving transducer digitizes the incident acoustic waveform on receiving transducer and the resulting data are saved on the laptop for postprocessing. Only data on the bovine samples are collected using the second setup.

The third setup [Fig. 1(c)], referred to from here on as the imaging setup, uses all the same hardware as setup one except the iris is removed to allow scanning of the generation laser spot. The beam diameter at the surface of the sample is 2 mm and the pulse energy is 0.8 mJ, yielding skin safe optical exposure levels from 810 to 2000 nm. The transducer position is now on the sample's top surface just like the generation laser spot. The data acquisition setup is identical to setup one. The sample under test is bovine shoulder muscle purchased from the butcher with two small metal wires inserted into it.

The data collection process using the imaging setup consists of scanning the generation laser a distance of 5.4 cm in the  $x$ -direction in 0.54-mm discrete steps along the sample surface starting 0.5 cm from the transducer [Fig. 1(c)]. At each of the 101 scan locations, the generation laser excites an LUS source and the transducer, which remains fixed for the scan, records the direct and reflected wave arrivals. Four scans using generation laser wavelengths of 810, 1064, 1550 and 2000 nm comprise the dataset from the imaging setup. The analog gain on the transducer remains constant across all scans. An SAFT algorithm<sup>10</sup> is used to generate an ultrasound image from each scan yielding four images from four different generation laser wavelengths on the same target.

## 3 Results

### 3.1 Waveforms and Spectra

The LUS source signals in the bovine sample, measured with experimental setup one, exhibit a similar form to LUS source signals observed in water<sup>11,12</sup> [Fig. 2(a)]. The data in Fig. 2(a) are from the bovine samples, data for the pork and chicken are similar and are shown in Sec. 6 Appendix. The spectra of the signals exhibit a peak near 1 MHz and a steady decay in amplitude until the noise floor of the data is reached, near 3.5 MHz, depending on the optical wavelength used [Fig. 2(b)]. The decay in the spectral amplitude with frequency [Fig. 2(b)] is not due to the transducer response, which is shown by the dashed line in Fig. 2(b). The downward slope of the spectra after the 1-MHz peak is roughly twice the expected value for acoustic power law absorption for bovine muscle of  $-2.9 \frac{\text{dB}}{\text{cm MHz}}$ .<sup>47</sup> There is also energy that arrives after the first peak in the time-domain signals [Fig. 2(a)], which suggests multiple scattering along the

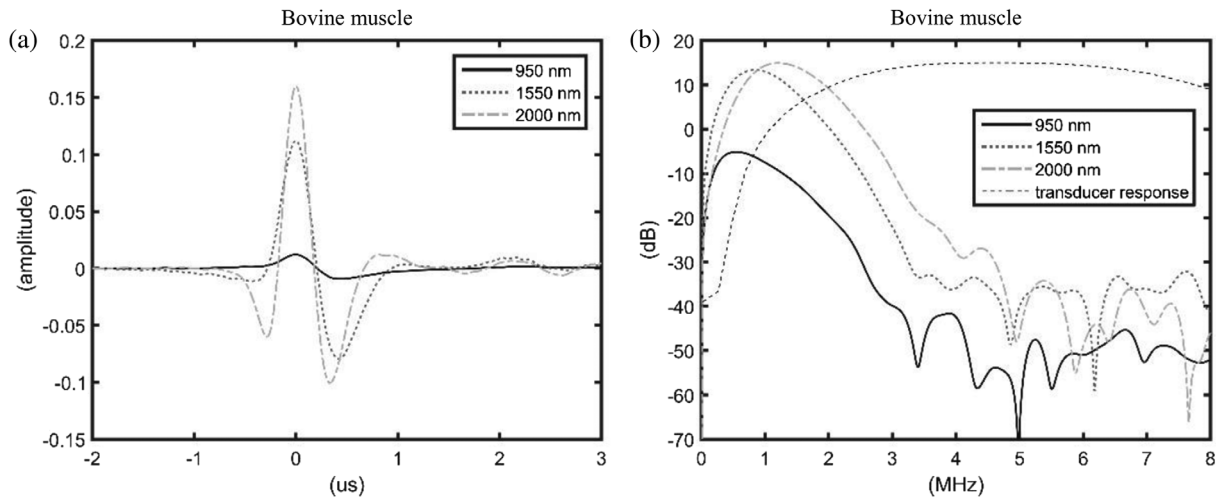


**Fig. 2** LUS source waveforms and spectra representative of the full dataset for the bovine sample. (a) LUS source waveforms collected from the bovine sample. (b) Spectra of the waveforms in (a) calculated with a Hanning window roughly over the  $-1$  to  $1 \mu\text{s}$  interval and the frequency response of the receiving transducer.

propagation path. It is also possible that scattering of the rough sample surfaces is accounting for the late arrival of energy.

The SNR of the waveforms collected from the chicken sample at the optical wavelengths of 800 and 850 nm is sufficiently low that the waveforms are excluded from the results. Waveforms from the pork sample at optical wavelengths of 800, 850, 900 and 950 nm are also excluded for the same reason. None of the waveforms collected on the bovine sample are excluded from the results.

### 3.2 Impact of Surface Roughness and Attenuation

The impact of surface roughness can be assessed by comparing waveforms collected using setup one (LUS source) with

waveforms from setup two (piezoelectric source). In Fig. 3(a), an LUS source signal generated with a 1550-nm pulse in a bovine sample (gray line) is compared with a signal generated by a piezoelectric transducer from setup two (thick black line). The signals are collected on the same sample along the same acoustic path using the same receiver. The LUS signal is also compared with theoretical predictions (thin black line and dashed line).

The theoretical prediction (thin black line) for the LUS source waveform using Eq. (6) is corrected for acoustic attenuation, surface roughness, and the transducer frequency response to best predict the observed data collected from the experimental setup and shows good agreement with the observed LUS source signal (gray line) [Figs. 3(a) and 3(b)]. As the acoustic data are

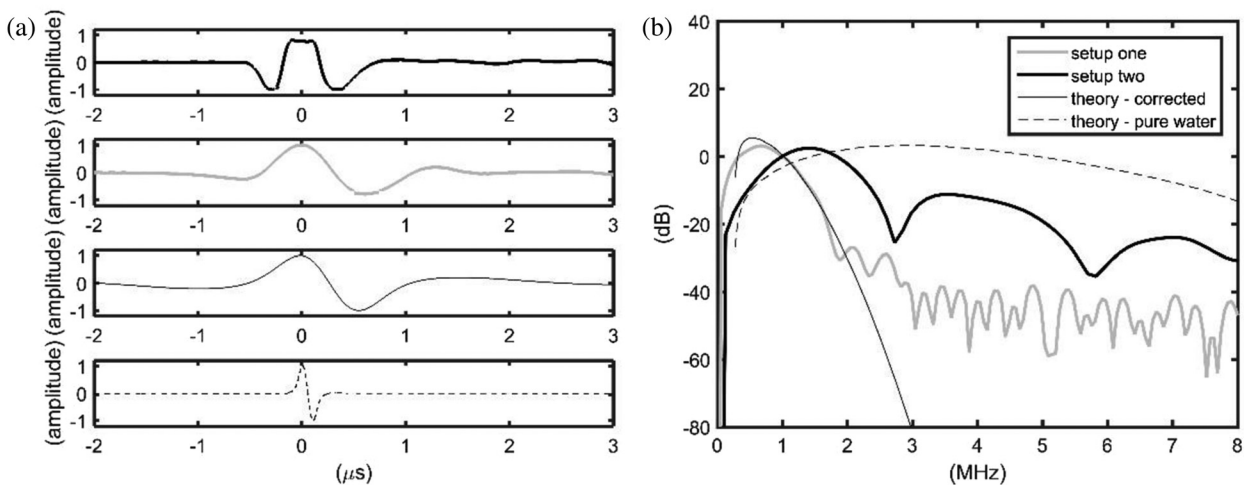


**Fig. 3** Time-domain waveforms and spectra from the bovine sample acquired using experimental setup one and two plotted with theoretical predictions. (a) Time-domain waveforms. The thick black line is the data from setup two using piezoelectric transducer to send and receive the acoustic signal. The gray line is the LUS source waveform acquired in the bovine sample with a 1550-nm wavelength optical pulse. The thin black line is Eq. (6) corrected for acoustic attenuation in bovine muscle ( $-2.9 \frac{\text{dB}}{\text{cm MHz}}$ ), the transducer response, and a surface roughness factor of  $\sigma = 3.4 \times 10^{-4}$  m. The dashed line is Eq. (5) corrected for the transducer response. (b) The spectra of the signals in (a) with the same line coding. Note the steeper decrease in signal amplitude with frequency for the data from experimental setup one (gray line) compared with setup two (thick black line).

not calibrated, Eq. (6) is arbitrarily shifted vertically to compare with the observed data. The key parameters put into the theoretical prediction are  $\mu_a = 730 \text{ m}^{-1}$ ,  $\sigma = 3.4 \times 10^{-4} \text{ m}$ , and  $\alpha = -2.9 \text{ dB/cm MHz}$ . The value for  $\sigma$  is the value that minimizes the mean square error between the model [Eq. (6)] and the data over the 0.5 to 2 MHz spectral band. The values for  $\mu_a$  and  $\alpha$  are taken from the literature.<sup>45,47</sup> The spectra of the time domain signals from Fig. 3(a) are shown in Fig. 3(b). Both spectra are sloping downward as expected. The negative slope of the spectra from setup one is significantly greater than the downward slope from setup two. As both signals experience the same acoustic attenuation, the results suggest surface roughness impacts the bandwidth of LUS signals. The nulls in the spectra from setup two at 2.75 and 5.75 MHz are intrinsic to a square pulse waveform. This comparison is not shown for other tissues because reliable estimates of  $\alpha$  for other tissues are not available in the literature.

The experimental LUS signal from the bovine sample in Figs. 3(a) and 3(b) shows agreement with the “corrected” theoretical curves and thus the hypothesis that acoustic absorption and surface roughness play a significant role determining the LUS source characteristics. The dashed lines in Figs. 3(a) and 3(b) are the theoretical prediction for an LUS source waveform generated on a smooth pure-water surface corrected only for the receiving transducer frequency response.

The experimental results are wider in the time domain [Fig. 3(a)] and narrower in the spectral domain [Fig. 3(b)] (gray line) compared with the theoretical predictions for pure water. This is due to surface roughness and attenuation that affect LUS source waveforms in biological tissues. Data collected on water, not shown, are similar to the theoretical curves with high SNR from 1 MHz up to 9 MHz as well as a narrow pulse.

### 3.2.1 Signal power as function of absorption

As shown in Eq. (5), the energy of the LUS source signal should strongly depend on  $\mu_a^2$  for the experiments conducted. As shown in Figs. 4(a)–4(c), the energy as a function of optical wavelength for each tissue closely follows the  $\mu_a^2$  curve for water. The energy of the LUS source signals from bovine, chicken, and pork samples as well as the energy compensated by the efficiency factor from Eq. (5) versus optical wavelength are shown in Figs. 4(a)–4(c) on a logarithmic scale. On the second y-axis,  $\mu_a^2$  for water<sup>45</sup> is plotted on a logarithmic scale [Figs. 4(a)–4(c)]. The energy of an LUS source signal is calculated by integrating the spectrum of each waveform in the 0.5- to 2.5-MHz band.

### 3.2.2 Impact of generation laser optical wavelength on image quality

The images formed, using an SAFT technique,<sup>10</sup> from the data collected using the third experimental setup clearly show the two rods imbedded in the bovine sample as well as the sample–table interface [Figs. 5(a)–5(d), Fig. 1(c)]. The brightness of the rod and sample–table interface increases with optical wavelength of the generation laser, illustrating a strong dependence of image SNR on the generation laser wavelength for biological tissues [Figs. 5(a)–5(d)]. The wires are the bright spots in the images at  $z = 2.25 \text{ cm}$  and  $z = 1.75 \text{ cm}$  and are indicated schematically by the green dots in Figs. 5(a)–5(d). The rod at  $z = 2.25 \text{ cm}$  is not perfectly perpendicular to the imaging plane and fades in and out of the image from  $x = 1.5$  to

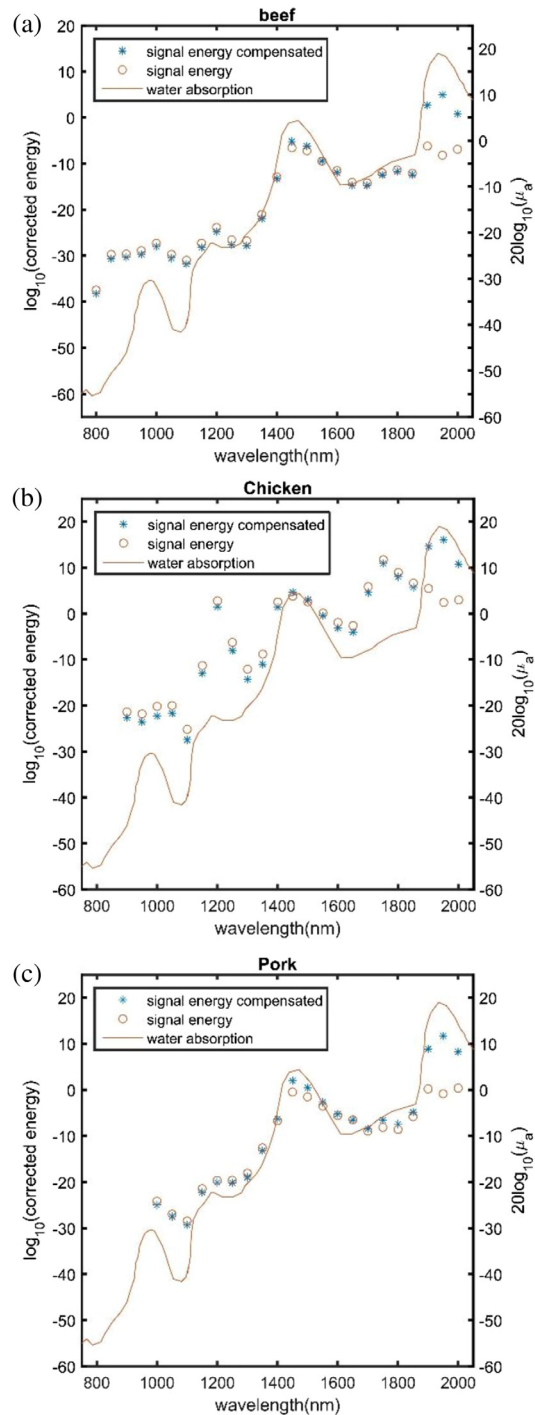


**Fig. 4** Dependence of signal energy uncorrected for efficiency; see Eq. (5) as a function of optical wavelength as compared with  $\mu_a$  of water for bovine, chicken, and pork samples. (a) Signal energy vs. optical wavelength for bovine sample. (b) Signal energy versus optical wavelength for chicken sample. (c) Signal energy versus optical wavelength for pork sample.

3.0 cm. The bright return at  $z = 4.0 \text{ cm}$  is the sample–table interface. The interface appears brighter than the rods despite being located at larger range, because it is a stronger reflector and scatterer of acoustic waves compared with the rods. The interface appears to lift and disappear for  $x > 3 \text{ cm}$ , this is likely due to side lobe interference and the specular reflections of the boundary. Specular reflections are not always imaged well using

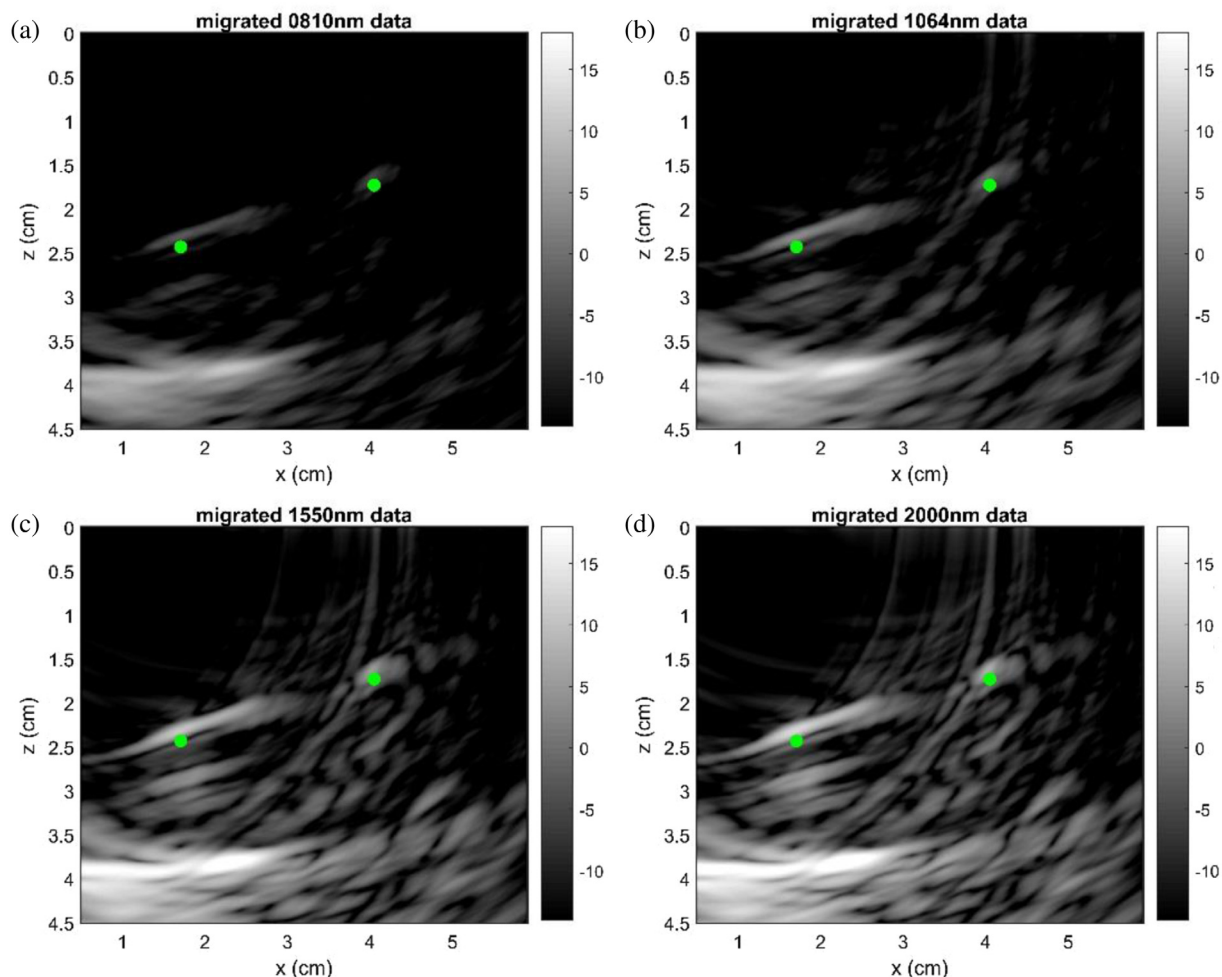


**Fig. 5** Dependence of image quality on the generation laser wavelength. All images are shown on a 32-dB dynamic range and are acquired on the same sample at the same location using identical fluences. The green dots indicate the approximate locations of the metal wires in the images. (a) Image resulting from the dataset using a 810-nm generation laser wavelength. (b) Image resulting from the data set using a 1064-nm generation laser wavelength (c) Image resulting from the dataset using a 1550-nm generation laser wavelength. (d) Image resulting from the dataset using a 2000-nm generation laser wavelength.

SAFT techniques because SAFT was developed for imaging point scatterers<sup>10</sup> like the rods. The energy in the image between the rods and the table is interference likely due to side lobes from the sample–table interface and internal reflections and mode conversion in the elastic rods. All images are acquired on the identical sample with matching scan patterns and displayed on matching color scales.

#### 4 Discussion

The waveform and spectral shapes of LUS source signals observed in the tissues tested are broadly consistent with the theory for LUS source signals in pure water (Fig. 2) when acoustic attenuation, surface roughness, and the receiving transducer response are taken into account [Figs. 3(a) and 3(b)]. Further analysis of the LUS source signals suggests that Eqs. (5) and (6) are valid for biological tissue at the optical wavelengths from 1400 to 1550 nm and 1900 to 2000 nm (Fig. 6). At these optical wavelengths,  $\mu_a$  is greater than  $\mu_s$ , which means the effect of scattering in the medium is small compared with absorption.<sup>45,46,50</sup> For the theoretical predictions in Fig. 6,

Eq. (6) is used with values of  $\mu_a$  taken from Ref. 51,  $\sigma = 1.5 \times 10^{-4}$  m and  $\alpha = -2.9$  dB/cm MHz and the theoretical curves are corrected by the receiving transducer frequency response.

The agreement between the model and measured data spectral slope [Figs. 3(a) and 3(b), Fig. 6] confirms the predictive power of the theoretical models. These models indicate that the spatial resolution of noncontact LUS imaging systems using a pulsed laser source is controlled by the roughness of the tissue surface and the acoustic attenuation of the tissue. The dependence of the LUS source on these parameters could result in patient and body-part-dependent resolution and system performance. These results also indicate that the resolution of a non-contact LUS imaging system will likely be better than 3 mm as there is always acoustic energy in the frequency range above 500 kHz (i.e.,  $\lambda = c/f$ ).

The relative energy in the observed LUS source waveforms for all three tissues agrees with the absorption curve for water [Figs. 4(a)–4(c)] as predicted by Eqs. (5) and (6), respectively. The optimal optical wavelengths for maximizing LUS source energy are from 1400 to 1550 nm as well as 1900 to 2000 nm [Figs. 4(a)–4(c)], consistent with Yao et al.<sup>32</sup>

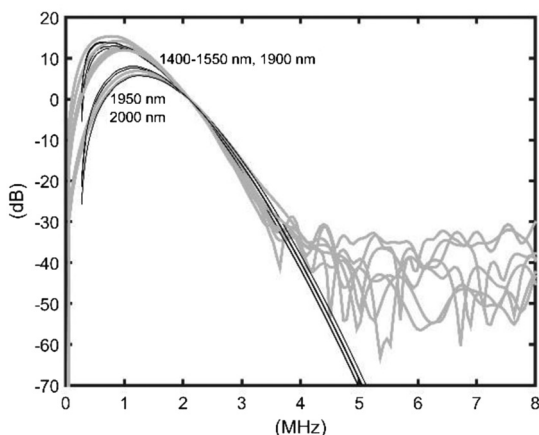


**Fig. 6** Spectra of LUS source signals from the bovine sample at optical wavelengths of 1400 to 1550 nm as well as 1900 to 2000 nm (gray lines) compared with theoretical predictions including surface roughness acoustic attenuation and transducer response (black lines). Note: the curves have been arbitrarily shifted vertically to show the agreement in the spectral slope (controlled by  $\sigma$  and  $\alpha$ ) between the observations and the theory.

These are ideal wavelength ranges to work with when developing noncontact LUS imaging systems for medical purposes. Optical hardware operating in these ranges is commonly available. Additionally, the high optical absorption values for water in these ranges could allow eye and skin safe designs with larger fluence levels compared with wavelengths  $<1400$  nm. At the frequencies of interest (0.5 to 5.0 MHz), the high optical absorption, safety thresholds, and source efficiency [Eq. (5)] in the 1400 to 1550 nm and 1900 to 2000 nm wavelength ranges (Fig. 7) allow for the largest safe LUS acoustic sources compared with any other wavelength bands. The optical absorption for water at 3000 nm is also high, but the efficiency for generating an acoustic source in the low MHz range is very low at this optical wavelength [see Eq. (5)].

These results additionally suggest that higher bandwidth ultrasonic signals can be generated in humans because the acoustic attenuation is typically  $0.5 \frac{\text{dB}}{\text{MHz}} \text{cm}$ , which is smaller than in bovine muscle. Additionally, the surface of human

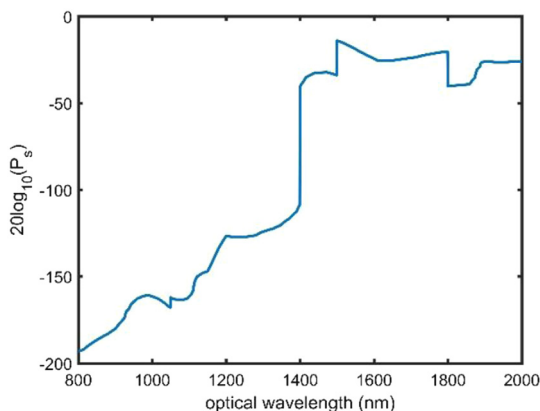


**Fig. 7** LUS source amplitude [Eq. (5)] at 1.5 MHz versus optical wavelength when accounting for ocular maximum permissible exposure<sup>49</sup> to a 1 ns to 1  $\mu$ s long pulse.  $U_o$  is taken from Ref. 47 and  $\mu_a$  from Ref. 49 and all other constants in Eq. (5) are set to 1. Note how significantly larger sources can be generated at wavelengths above 1400 nm at safe optical exposure levels.

skin in many cases will be smoother than the surface of the samples tested here. Measurements on human subjects *in vivo* are not done for this study due to the difficulty in obtaining a measurement location with an unimpeded acoustic path and concerns of reliably and safely aligning the LUS source location and the receiver. Mouse experiments are also avoided due to the lack of a predominantly homogenous propagation path of  $>2.5$  cm to obtain far-field measurements. Future work should include measurements *in vivo* and *ex vivo* on human tissue and, where appropriate, measurements in mouse models.

Lastly, it is seen [Figs. 5(a)–5(d)] that the image quality improves with increasing optical wavelength of the generation laser, consistent with the results showing energy in the LUS source wave increases with increasing optical wavelength of the generation laser. These images demonstrate the importance of choosing a generation laser wavelength to maximize image quality by maximizing the source amplitude. In the context of designing a noncontact LUS system for imaging biological tissue, one should choose a generation laser wavelength where the absorption coefficient of water and the acceptable human exposure limits are high to generate the largest amplitude LUS source possible. In cases where treatment of the sample surface is acceptable, it may be advantageous to use films designed to have large optical absorption and thermal expansion coefficients.<sup>25–29</sup>

## 5 Conclusion

LUS sources are generated using a pulsed laser at optical wavelengths from 800 to 2000 nm, with 50-nm increments, in bovine, chicken, and pork tissue samples, to assess the relevant theory and constraints for choosing an optimal generation laser wavelength for a noncontact, nonimmersion, and surface treatment free LUS imaging system. The data can be used as a reference dataset for future design of noncontact LUS imaging systems for biological tissue. The resulting dataset also expands the number of optical wavelengths and tissues for which LUS signals have been excited and recorded in the far field. Optical wavelengths from 1400 to 1550 nm and from 1900 to 2000 nm are likely to be good choices for a medical noncontact LUS imaging system. The results also show the majority of LUS signal energy in biological tissues is within the 0.5- and 3-MHz frequency band for most of the generation laser optical wavelengths tested. Experimental results suggest that, for system design purposes, it is appropriate to model LUS source signals in biological tissues using the LUS theory for pure water and correcting for surface roughness and acoustic attenuation. This is not a perfect approximation, and there are cases where it is not appropriate, especially if predicting absolute source amplitude. A factor not addressed is the optically inhomogeneous nature of biological tissue, which likely further reduces the signal amplitude due to reduced absorption and increased scattering as well as modifies the signal bandwidth and even modifies the shape of the signal.

## 6 Appendix

This appendix presents the data from the pork and chicken samples [Figs. 8(a)–8(d)]. The waveforms and spectra are similar to those for the bovine sample. A skin layer is present on both the chicken and the pork samples yet the presence of the skin does not appear to alter the source waveform characteristics compared with the beef sample.

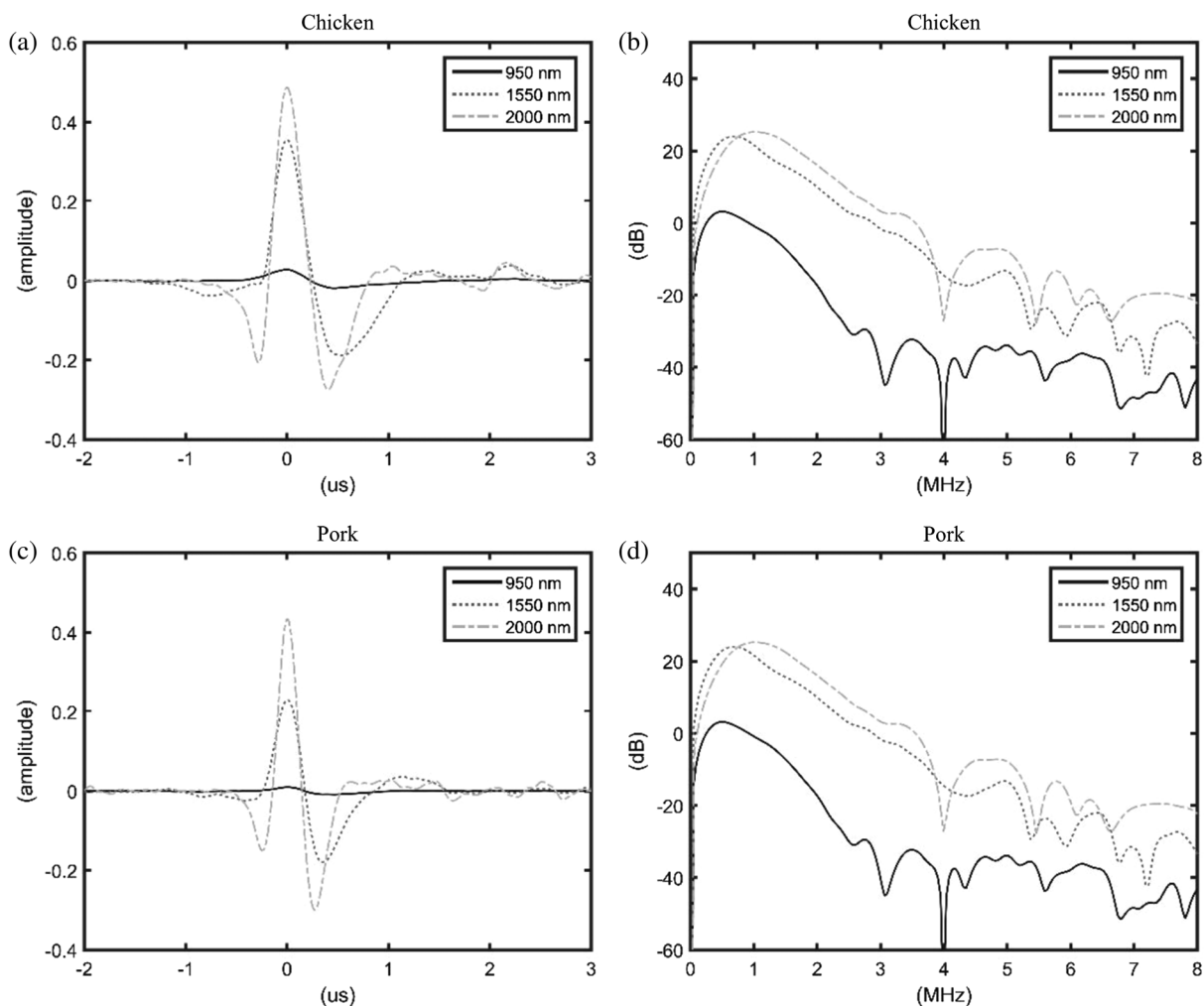


**Fig. 8** Acoustic waveforms and spectra representative of the full data set for the chicken and pork samples. (a) Acoustic waveforms collected from the chicken sample. (b) Spectra of the waveforms in (a) calculated with a Hanning window roughly over the  $-1$  to  $1 \mu\text{s}$  interval. (c) Acoustic waveforms collected from the pork sample. (d) Spectra of the waveforms in (c) calculated with a Hanning window roughly over the  $-1$  to  $1 \mu\text{s}$  interval.

### Disclosures

The authors have no relevant financial interests in this article and no potential conflicts of interest to disclose.

### Acknowledgments

This work was supported by the Massachusetts Institute of Technology Lincoln Laboratory Biomedical Line Program for the United States Air Force. This work was supported under Air Force Contract Nos. FA8721-05-C-0002 and/or FA8702-15-D-0001. Any opinions, findings, conclusions, or recommendations expressed in this material are those of the authors and do not necessarily reflect the views of the U.S. Air Force. Notwithstanding any copyright notice, U.S. Government rights in this work are defined by DFARS 252.227-7013 or DFARS 252.227-7014 as detailed above. Use of this work other than as specifically authorized by the U.S. Government may violate any copyrights that exist in this work.

### References

- J. H. Yoon et al., "Interobserver variability of ultrasound elastography: how it affects the diagnosis of breast lesions," *Am. J. Roentgenol.* **196**(3), 730–736 (2011).
- M. W. Gilbertson and B. W. Anthony, "Force and position control system for freehand ultrasound," *IEEE Trans. Rob.* **31**(4), 835–849 (2015).
- A. J. Pigula-Tresansky et al., "Muscle compression improves reliability of ultrasound echo intensity," *Muscle Nerve* **57**, 423–429 (2018).
- M. Pithioux, P. Lasaygues, and P. Chabrand, "An alternative ultrasonic method for measuring the elastic properties of cortical bone," *J. Biomech.* **35**(7), 961–968 (2002).
- S. C. Oltmann et al., "All thyroid ultrasound evaluations are not equal: sonographers specialized in thyroid cancer correctly label clinical N0 disease in well differentiated thyroid cancer," *Ann. Surg. Oncol.* **22**(2), 422–428 (2015).
- C. Li, N. Duric, and L. Huang, "Clinical breast imaging using sound-speed reconstructions of ultrasound tomography data," *Proc. SPIE* **6920**, 692009 (2008).
- K. Bredahl et al., "Reproducibility of ECG-gated ultrasound diameter assessment of small abdominal aortic aneurysms," *Eur. J. Vasc. Endovasc. Surg.* **45**(3), 235–240 (2013).
- C. B. Scruby and L. E. Drain, *Laser Ultrasonics Techniques and Applications*, 1st ed., Taylor and Francis Group, New York (1990).
- J.-P. Monchalain, "Laser-ultrasonics: from the laboratory to industry," in *AIP Conf. Proc.*, Vol. 700, pp. 3–31 (2004).
- D. Lévesque et al., "Performance of laser-ultrasonic F-SAFT imaging," *Ultrasonics* **40**(10), 1057–1063 (2002).

11. W. E. Gusev and A. A. Karabutov, *Laser Optoacoustics*, American Institute of Physics, Melville, New York (1993).
12. L. M. Lyamshev, *Radiation Acoustics*, CRC Press LLC, Boca Raton, Florida (2000).
13. J. P. Monchalin, "Optical detection of ultrasound," *IEEE Trans. Ultrason. Ferroelectr. Freq. Control* **33**(5), 485–499 (1986).
14. J. Eom et al., "Fiber-based dual modal system for noncontact photoacoustic and optical coherence tomography," *11th Conf. Lasers Electro-Optics Pacific Rim, CLEO-PR 2015*, Vol. 2, pp. 1–2 (2016).
15. A. Hochreiner et al., "Non-contact photoacoustic imaging using a fiber based interferometer with optical amplification," *Biomed. Opt. Express* **4**(11), 2322–2331 (2013).
16. A. Blouin et al., "Differential confocal Fabry–Perot for the optical detection of ultrasound," in *AIP Conf. Proc.*, Vol. 894, pp. 193–200 (2007).
17. M. Xu and L. V. Wang, "Photoacoustic imaging in biomedicine," *Rev. Sci. Instrum.* **77**(4), 041101 (2006).
18. J. L. Johnson, J. Shragge, and K. van Wijk, "Image reconstruction of multi-channel photoacoustic and laser-ultrasound data using reverse time migration," *Proc. SPIE* **9323**, 932314–932320 (2015).
19. J. L. Johnson, K. van Wijk, and M. Sabick, "Characterizing phantom arteries with multi-channel laser ultrasonics and photo-acoustics," *Ultrasound Med. Biol.* **40**(3), 513–520 (2014).
20. J. L. Johnson et al., "Gas-coupled laser acoustic detection as a non-contact line detector for photoacoustic and ultrasound imaging," *J. Opt.* **18**(2), 024005 (2016).
21. G. Rousseau, A. Blouin, and J.-P. Monchalin, "Non-contact photoacoustic tomography and ultrasonography for tissue imaging," *Biomed. Opt. Express* **3**(1), 16–25 (2012).
22. H. Wang et al., "Laser ultrasonic evaluation of human dental enamel during remineralisation treatment," *Biomed. Opt. Express* **2**(18), 345–355 (2011).
23. J. L. Johnson et al., "Ultrasound and photoacoustic imaging system for angle-dependent deep tissue imaging," *J. Biomed. Opt.* **22**(4), 041014 (2017).
24. J. L. Johnson et al., "All-optical extravascular laser-ultrasound and photoacoustic imaging of calcified atherosclerotic plaque in excised carotid artery," *Photoacoustics* **9**, 62–72 (2018).
25. J. Jose et al., "Passive element enriched photoacoustic computed tomography (PER PACT) for simultaneous imaging of acoustic propagation properties and light absorption," *Opt. Express* **19**(3), 2093–2104 (2011).
26. H.-P. Brecht et al., "Whole-body three-dimensional optoacoustic tomography system for small animals," *J. Biomed. Opt.* **14**(6), 064007 (2009).
27. S. A. Ermilov et al., "Three-dimensional optoacoustic and laser-induced ultrasound tomography system for preclinical research in mice: design and phantom validation," *Ultrason. Imaging* **38**(1), 77–95 (2016).
28. A. S. Bychkov et al., "Photoacoustics On the use of an optoacoustic and laser ultrasonic imaging system for assessing peripheral intravenous access," *Photoacoustics* **5**, 10–16 (2017).
29. A. Conjusteau et al., "Measurement of the spectral directivity of optoacoustic and ultrasonic transducers with a laser ultrasonic source," *Rev. Sci. Instrum.* **80**(9), 093708 (2009).
30. A. A. Oraevsky et al., "Direct measurement of laser fluence distribution and optoacoustic imaging in heterogeneous tissues," *Proc. SPIE* **2323**(7 13), 37–46 (1995).
31. A. A. Oraevsky, S. L. Jacques, and F. K. Tittel, "Measurement of tissue optical properties by time-resolved detection of laser-induced transient stress," *Appl. Opt.* **36**(1), 402 (1997).
32. D.-K. Yao et al., "Photoacoustic measurement of the Grüneisen parameter of tissue," *J. Biomed. Opt.* **19**(1), 017007 (2014).
33. B. Choi, D. E. Jansen, and A. J. Welch, "Acoustic-based measurements of material absorption coefficients: relationship between laser pulse duration and stress confinement time," *J. Appl. Phys.* **94**(12), 7826–7831 (2003).
34. G. Paltauf and H. Schmidt-Kloiber, "Photoacoustic determination of tissue optical properties and structure by use of an optical parametric oscillator," *Proc. SPIE* **3195**, 70–78 (1998).
35. K. P. Köstli et al., "Optoacoustic infrared spectroscopy of soft tissue," *J. Appl. Phys.* **88**(3), 1632–1637 (2000).
36. L. Liamshev and L. Sedov, "Optical generation of sound in a liquid-thermal mechanism/review," *Akust. Zhurnal* **27**(1), 4–18 (1981).
37. L. M. Lyamshev, "Optoacoustic sources of sound," *Uspekhi Fiz. Nauk* **135**(12), 637 (1981).
38. M. L. Lyamshev, V. G. Mikhalevich, and G. P. Shipulo, "Thermo-optical excitation of acoustic fields in a liquid by a periodic train of laser pulses," *Sov. Phys. Acoust.* **26**(2), 126–130 (1980).
39. A. D. Pierce, "The inhomogeneous wave equation of thermoacoustics," *Lect. Notes Phys.* **235**, 92–100 (1985).
40. Y. Berthelot and I. Busch-Vishniac, "Laser-induced thermoelastic radiation," *J. Acoust. Soc. Am.* **78**(6), 2074–2082 (1985).
41. T. G. Muir, C. R. Culbertson, and J. R. Clynch, "Experiments on thermoacoustic arrays with laser excitation," *J. Acoust. Soc. Am.* **59**(4), 735–743 (2016).
42. S. V. Egerev et al., "Sound generation by long laser pulses," *Sov. Phys. Acoust.* **25**(2), 119–122 (1979).
43. T. Szabo, *Diagnostic Ultrasound Imaging*, Elsevier Science, Amsterdam, The Netherlands (2004).
44. A. A. Oraevsky et al., "Lateral and z-axis resolution in laser optoacoustic imaging with ultrasonic transducers," *Proc. SPIE* **2389**(198), 198–208 (1995).
45. S. L. Jacques, "Optical properties of biological tissues: a review," *Phys. Med. Biol.* **58**(14), 5007–5008 (2013).
46. T. L. Troy and S. N. Thennadil, "Optical properties of human skin in the near infrared wavelength range of 1000 to 2200 nm," *J. Biomed. Opt.* **6**(2), 167–176 (2001).
47. D. Shore, M. O. Woods, and C. A. Miles, "Attenuation of ultrasound in post rigor bovine skeletal muscle," *Ultrasonics* **24**(2), 81–87 (1986).
48. F. A. Duck, *Physical Properties of Tissue*, 1st ed., Academic Press Limited, London (1990).
49. Lasers Institute of America, *American National Standard for Safe Use of Lasers* (2007).
50. B. Chance et al., "Phase measurement of light absorption and scatter in tissue," *Rev. Sci. Instrum.* **69**(10), 3457–3481 (1998).
51. G. M. Hale and M. R. Querry, "Optical constants of water in the 200 nm to 200 mm wavelength region," *Appl. Opt.* **12**(3), 555–563 (1973).

**Jonathan R. Fincke** received his BS degree in mechanical engineering from the University of New Hampshire, his MS degree in oceanographic engineering from the MIT/WHOI Joint Program, and his PhD from Massachusetts Institute of Technology in mechanical engineering. His research includes the development of systems and algorithms for noncontact quantitative ultrasound imaging of soft tissue and bone.

**Charles M. Wynn** is a research scientist at MIT Lincoln Laboratory. Currently, he is leading efforts focused on laser-based trace detection and hyperspectral imaging. Additional research interests include molecular electronics, low-light imaging systems, and microwave spectroscopy of left-handed metamaterials. He was the winner of an R&D 100 Award and was a finalist for two others. He has three patents and more than 30 scientific publications including a book chapter on trace explosives detection.

**Rob Haupt** is a technical staff member at the MIT Lincoln Laboratory in the Active Optical Systems Group. His research focuses on coherent laser radar for vibration imaging and material property quantification. His research encompasses noncontact laser ultrasound, photoacoustic detection of explosives, seismic cloaking, and seismic detection of buried land mines using laser vibrometry. He completed his graduate studies in geophysics at Penn State and mechanical engineering at Dartmouth College.

**Xiang Zhang** received his undergraduate degree in mechanical engineering from the University of Maryland-College Park (UMCP); during which he completed a co-op at National Institute of Standards and Technology (NIST). Currently, he completed his master's degree and is continuing for his PhD in mechanical engineering at MIT, advised by Dr. Brian Anthony. His research focuses on design of electromechanical systems to enhance medical ultrasound, 3-D tomographic ultrasound for tissue property characterization, and non-contact laser ultrasound.

**Diego Rivera** is an assistance staff member at MIT LL working for the Active Optical Systems Group as software engineer and technical leader in projects related with lidar processing. He is a graduate of

the University of Cauca (BSEE), University of Puerto Rico (MSEE), and Northeastern University (MSCE).

**Brian Anthony** is a principal research scientist at the Department of Mechanical Engineering and the Institute for Medical Engineering and Science (IMES), Massachusetts Institute of Technology, Cambridge,

MA, USA. Currently, he is a codirector of the Medical Electronics Device Realization Center (MEDRC) and director of the Master of Engineering in Manufacturing (MEngM) Program. His research includes the development of instrumentation and measurement solutions for manufacturing systems, medical diagnostics, and imaging systems.